ISSN 1063-7761, Journal of Experimental and Theoretical Physics, 2017, Vol. 124, No. 3, pp. 476–492. © Pleiades Publishing, Inc., 2017.
Original Russian Text © N.A. Grigor'eva, H. Eckerlebe, A.A. Eliseev, A.V. Lukashin, K.S. Napol'skii, M. Kraje, S.V. Grigor'ev, 2017, published in Zhurnal Eksperimental'noi i Teoreticheskoi Fiziki, 2017, Vol. 151, No. 3, pp. 558–577.

ORDER, DISORDER, AND PHASE TRANSITION IN CONDENSED SYSTEM

Structural and Magnetic Properties of the Nanocomposite Materials Based on a Mesoporous Silicon Dioxide Matrix

N. A. Grigor'eva[a]*, H. Eckerlebe[b], A. A. Eliseev[c], A. V. Lukashin[c], K. S. Napol'skii[c], M. Kraje[d], and S. V. Grigor'ev[a,e]

[a] *St. Petersburg State University, ul. Ul'yanovskaya 3, Petrodvorets, St. Petersburg, 198504 Russia*
[b] *Helmholtz-Zentrum Geesthacht 2150, Geesthacht, Germany*
[c] *Moscow State University, Moscow, 119991 Russia*
[d] *Reactor Institute Delft 2629 JB, Delft, The Netherlands*
[e] *B. P. Konstantinov Petersburg Nuclear Physics Institute, Russian Academy of Sciences, ul. Orlova Roshcha 1, Gatchina, Leningradskaya oblast, 188300 Russia*
**e-mail: natali@lns.pnpi.spb.ru*

Received March 15, 2013; in final form, October 11, 2016

Abstract—The structural and magnetic properties of the mesoporous systems based on silicon dioxide with a regular hexagonal arrangement of pores several microns in length and several nanometers in diameter, which are filled with iron compound nanofilaments in various chemical states, are studied in detail. The studies are performed using the following mutually complementary methods: transmission electron microscopy, SQUID magnetometry, electron spin resonance, Mössbauer spectroscopy, polarized neutron small-angle diffraction, and synchrotron radiation diffraction. It is shown that the iron nanoparticles in pores are mainly in the γ phase of Fe_2O_3 with a small addition of the α phase and atomic iron clusters. The effective magnetic field acting on a nanofilament from other nanofilaments is 11 mT and has a dipole nature, the ferromagnetic–paramagnetic transition temperature is in the range 76–94 K depending on the annealing temperature of the samples, and the temperature that corresponds to the change in the magnetic state of the iron oxide nanofilaments is $T \approx 50$–60 K at $H = 0$ and $T \approx 80$ K at $H = 300$ mT. It is also shown that the magnetization reversal of an array of nanofilaments is caused by the magnetostatic interaction between nanofilaments at the fields that are lower than the saturation field.

DOI: 10.1134/S106377611702011X

1. INTRODUCTION

Over the last decades, new magnetic materials, which make it possible to increase the density of data recording and storage due to a decrease in the bit size, have been actively implemented due to the development of computation engineering. High-quality nanostructures with given characteristics are promising materials for the production of memory devices with an ultrahigh data recording density [1, 2]. However, a decrease in the magnetic bit size down to atomic scales raises new problems. First, the contributions of the specific surface area and the related excess surface energy to the physicochemical properties of a system increase, which leads to an increase in the chemical activity and the enhancement of nanoparticle aggregation. Second, nanoparticles exhibit superparamagnetic behavior, i.e., thermal fluctuations of the magnetization vector of a nanoparticle; therefore, it cannot be used as an information storage bit. Third, the existence of contacts between magnetic particles causes rather strong exchange and dipole interactions, which result in correlated behavior of the magnetic moments of neighboring grains during magnetization reversal. To solve these problems, technologists use the approach related to the formation of nanocomposite materials based on chemically inert matrices, which makes it possible to separate magnetic particles from each other mechanically, to avoid the influence of exchange forces and nanoparticle aggregation, and to protect them from external actions. One of the promising chemically inert matrices is represented by amorphous silicon dioxide SiO_2 with a controlled distribution of pores over the volume and a high specific porosity. The structure, the pore size, and the pore distribution in a matrix are controlled by the use of various templates during synthesis. Several types of mesoporous matrices synthesized using liquid-crystal templates are known [3]. Mesoporous systems with a regular hexagonal distribution of pores several microns in length and several nanometers in diameter have the maximum anisotropy constant and can be considered as one-dimensional (1D) matrices. It is obvious that, when nanoparticles form in such matri-

ces, their size and shape are determined by the pore morphology. Some attempts have been recently made to synthesize metallic nanowires in a mesoporous silicon oxide matrix via the impregnation of SiO_2 in metal salt solutions followed by the reduction of metal cations [4]. However, these methods turned out to be improper for the fabrication of filament nanoparticles because of the high mobility of cations along silanol groups on the inner pore surface and, hence, nanoparticle formation on the surface of mesoporous silicon oxide "crystallites."

To synthesize ordered magnetic iron nanowires embedded in a mesoporous silicon oxide matrix, a nonpolar metal complex was introduced into the hydrophobic part of a mesoporous template/SiO_2 composite material [5]. As the nonpolar metal complex, iron pentacarbonyl $Fe(CO)_5$ was chosen since it can be easily decomposed to elementary iron by simple ultraviolet irradiation in vacuum or by thermal decomposition. Samples were additionally annealed in a hydrogen flow to ensure the crystallization of iron compounds inside matrix channels. The structural and magnetic properties of the nanocomposite materials based on a mesoporous silicon oxide matrix with embedded iron nanoparticles were analyzed by the following mutually complementary methods: transmission electron microscopy (TEM), synchrotron radiation diffraction (XRD), Mössbauer spectroscopy, electron spin resonance (ESR), SQUID magnetometry, and small-angle polarized-neutron scattering (SAPNS). We studied (i) the spatial distribution of pores in the matrix volume by TEM, SAPNS, and XRD; (ii) the filling of pores with nanoparticles, the nanofilament sizes, and the anisotropy parameters by SAPNS, SQUID magnetometry, TEM; (iii) the crystal structure and the phase composition of the filling material by XRD, ESR, and Mössbauer spectroscopy; (iv) the state of the silicon dioxide/iron-containing nanofilament interface by SAPNS, ESR, and TEM; and (v) the magnetic properties of iron-containing nanofilaments as functions of the applied magnetic field and temperature by SAPNS and SQUID magnetometry.

2. SAMPLES

A mesoporous silicon oxide matrix was synthesized by the polycondensation of a silicon source in the presence of a template. As the template, we used cetyltrimethylammonium bromide $C_{16}H_{33}$ (TMABr). The bifunctional molecules of this substance are amphiphilic; that is, they contain a hydrophilic head group and a hydrophobic tail. Therefore, micelles, where hydrophilic head groups form an outer surface and hydrophobic tails are directed toward the center, form in an aqueous solution. The degree of micelle formation and the micelle shape depend on the surfactant concentration. As a silicon source, we used tetrasthoxysilane ($Si(C_2H_5O)_4$, TEOS). The reaction mixture contained an aqueous solution of surfactant, TEOS, and ammonia and was stored in a thermostat at room temperature for several hours. The molar ratio of the components was 1 M TEOS : 0.152 M CTAB : 2.8 M NH_3 : 141.2 M H_2O. In this case, mesoporous silicon oxide forms around surfactant micelles as a result of the hydrolysis of tetrasthoxysilane. The solution was then filtered, and the filter cake was washed by distilled water and dried in air at room temperature. Iron pentacarbonyl $Fe(CO)_5$ was introduced into the hydrophobic part of the template/SiO_2 composite material by the impregnation of about 1 g dried mesoporous silicon oxide with 10 mL liquid iron carbonyl. The sample was then filtered with a paper filter and washed with hexane to remove iron carbonyl from the surface of mesoporous SiO_2. All operations were performed in an argon atmosphere. The carbonyl complex was decomposed by ultraviolet (UV) irradiation in a vacuum of 10^{-2} mmHg for 10 h (1000-W DRT-1000 lamp). Iron nanoparticles were crystallized upon annealing of the sample in a hydrogen flow at a flow rate of 50–70 mL/min and a temperature $T = 250$, 300, 350, 375, and 400°C for 3 h. The synthesized powdered samples were designated as Fe–SiO_2–UV (sample subjected to UV radiation and unannealed), Fe–SiO_2–250, Fe–SiO_2–300, Fe–SiO_2–350, Fe–SiO_2–375, and Fe–SiO_2–400 (number stands for the annealing temperature).

3. ANALYSIS OF THE STRUCTURAL PROPERTIES OF THE NANOCOMPOSITE MATERIALS BASED ON A MESOPOROUS SILICON DIOXIDE MATRIX

3.1. Electron Microscopy

Micrographs of the structures of the samples were taken with a JEOL JEM-2000FXII transmission electron microscope at an accelerating voltage of 200 kV and a magnification of 1000–400000. Figure 1 shows typical TEM micrographs and electron diffraction patterns of the nanocomposites Fe–SiO_2–350 (Fig. 1a), Fe–SiO_2–375 (Fig. 1b), and Fe–SiO_2–400 (Fig. 1c), which demonstrate a periodic nanopore structure. The electron diffraction pattern of the structured silicon oxide matrix in the sample annealed at 350°C has three orders of diffraction rings, the sample annealed at 375°C has four orders of diffraction rings, and that annealed at 400°C has two orders (insets to Fig. 1). The diffraction rings in the last case are strongly broadened. This difference can be explained by, first, the exit of residual carbon atoms, which formed in SiO_2 matrix pores after the decomposition of the pentacarbonyl complex under UV radiation, when the annealing temperature increases from 350 to 375°C, which leads to higher contrast in TEM micrographs. Second, as the annealing temperature increases to 400°C, the ordered structure of pores is

partly broken because of the "melting" of embedded nanofilaments, which brings about an increase in the mobility of introduced atoms and, hence, a tendency toward decreasing the surface energy. In other words, the morphology of nanofilaments changes from a filament to a droplike shape [6]. Using the TEM data, we can determine the structure periodicity in the SiO_2 matrix ($a_0 = 4.4 \pm 0.2$ nm), the pore diameter ($D =$ ~2 nm), and the filament lengths. These lengths are several tens of nanometers in the Fe–SiO_2–350 and Fe–SiO_2–400 samples and are $L > 100$ nm in the Fe–Fe–SiO_2–375 sample (dark bands in Fig. 1). Apart from the rings corresponding to the ordered two-dimensional structure of SiO_2 matrix pores, the electron diffraction patterns of the samples also contain point reflections of structured clusters made of the introduced material. The number of such reflections increases noticeably with the annealing temperature.

We have deliberately avoided using the exact name of the material embedded into matrix pores. Based on the data analysis of other authors and common sense, one should proceed from the assumption that both "crystalline" and "amorphous" phases could be formed within the pores as a result of the chemical synthesis and subsequent modification by ultraviolet and thermal irradiation. Here, the latter phase is most probable due to insufficiently high annealing temperatures and small pore size. Indeed, the formed nanofilaments have a diameter of at most 2 nm. This means that, at an iron atomic radius of 0.126 nm, about 50% of the iron atoms are on the nanofilament surface with broken chemical bonds. As for chemical composition, both the crystalline and amorphous phases can contain iron (α-Fe) nanoparticles and iron oxide (oxidation level of +3) nanoparticles. The properties of amorphous (as determined by XRD) Fe_2O_3 and its four polymorphic modifications (α, β, γ, ϵ) in bulk and nanosized samples were described in detail in [7–13]. α-Fe_2O_3 (hexagonal structure) and γ-Fe_2O_3 (cubic structure) are abundant in nature. γ-Fe_2O_3 and ϵ-Fe_2O_3 (orthorhombic structure) are ferromagnets, α-Fe_2O_3 is an antiferromagnet, and β-Fe_2O_3 (cubic structure) is a paramagnet. The magnetic moment of bulk α-Fe_2O_3 is very low (about $1 \times 4\pi \times 10^{-3}$ A m^2/kg) as compared to γ-Fe_2O_3 (about $430 \times 4\pi \times 10^{-3}$ A m^2/kg) at room temperature. Below $T = 960$ K, bulk α-Fe_2O_3 samples exhibit weak ferromagnetism down to $T =$ 260 K (weak ferromagnet–antiferromagnet Morin transition) because of the rotation of antiferromagnetically arranged spins by 5°. γ-Fe_2O_3 nanoparticles also undergo the Morin transition; however, as the particle size decreases, the transition temperature decreases and disappears in particles smaller than 8 nm in diameter [14–16]. Thus, one of the aims of this work is to determine the phase composition of the introduced material.

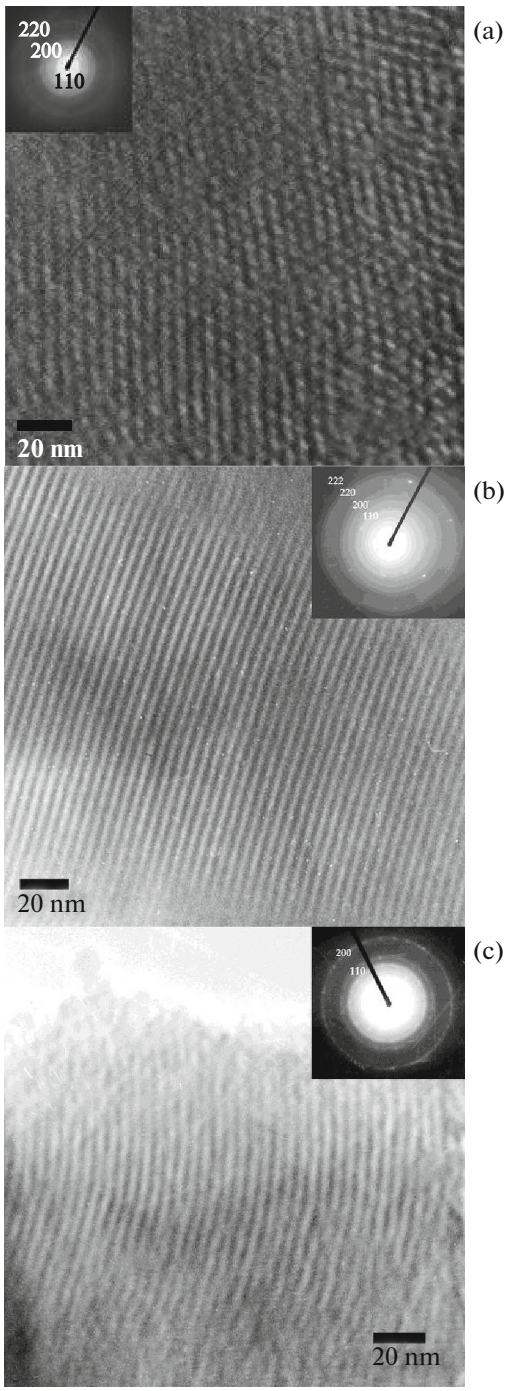

Fig. 1. TEM and the electron diffraction map of nanocomposites (a) Fe–SiO_2–350, (b) Fe–SiO_2–375, and (c) Fe–SiO_2–400.

3.2. Synchrotron Radiation Diffraction

Synchrotron radiation diffraction measurements were carried out in Swiss–Nerwegian Beamline BM01A of the European Synchrotron Radiation Facility (Grenoble, France) using a MAR345 position-sensitive detector in in-situ and ex-situ experiments. In the first case, Fe–SiO_2–UV samples were

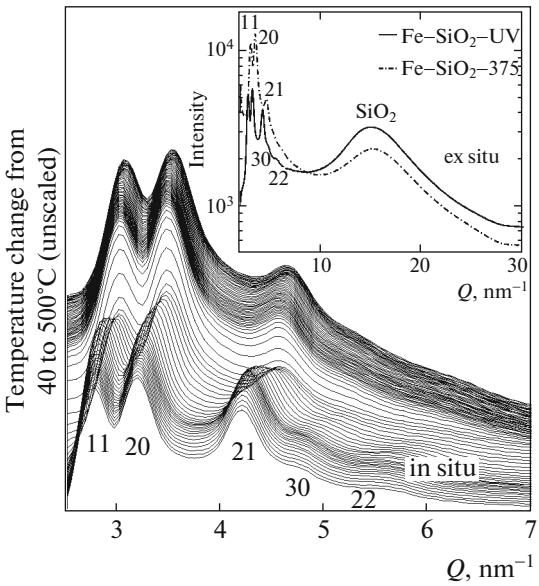

Fig. 2. Synchrotron radiation diffraction vs. transferred momentum Q for the Fe–SiO_2–UV and Fe–SiO_2–375 samples at $T = 300$ K (inset) and the Fe–SiO_2–UV sample annealed in a reducing atmosphere at 40°C < T < 500°C.

placed in a synchrotron radiation beam and were measured during annealing in a reducing atmosphere to prevent possible oxidation. In the second case, ready Fe–SiO_2–250, Fe–SiO_2–300, Fe–SiO_2–350, Fe–SiO_2–375, and Fe–SiO_2–400 samples were measured at room temperature. The X-ray radiation wavelength was $\lambda = 0.71118$ Å and the distance from a sample to the detector was $D = 350$ mm. The detector parameters were preliminarily calibrated against the diffraction spectra of lanthanum hexaboride (NIST standard 600). The measurement time was 3 min. The experimental results were processed with the FIT2D software package [17].

Figure 2 shows the synchrotron radiation intensity versus the transferred momentum for the Fe–SiO_2–UV and Fe–SiO_2–375 samples in ex-situ experiments and for the Fe–SiO_2–UV sample annealed in a reducing atmosphere at 40°C < T < 500°C during in-situ experiments.

The spectra of the samples consist of diffraction peaks, which correspond to the ordered structure of pores in a mesoporous matrix (low values of Q), and a halo from amorphous silicon oxide at $Q \approx 30$ nm^{-1}. The Bragg peaks in both ex- and in-situ experiments are strongly broadened. The peak corresponding to reflection of type 10 is in the range $Q < 2$ nm^{-1} (outside the region shown in Fig. 2). It is seen that the annealed samples exhibit faster decay of Bragg peaks with increasing Q than the unannealed samples do. For example, diffraction peaks 30 and 22 are very weak for the samples annealed at temperatures above T = 300°C and are clearly visible for Fe–SiO_2–UV. These facts point to an increase in the disorder in the structure of the mesoporous matrix in the Fe–SiO_2–T nanocomposites with increasing temperature. As compared to the unannealed Fe–SiO_2–UV sample, the diffraction peaks shift toward high Q when the annealing temperature increases, which indicates sintering of the matrix and a decrease in lattice parameter a_0. The parameters of the diffraction peaks were refined using the Winplotr software package (Table 1) [18]. A pseudo-Voigt function was used as a model. The arrangement of the diffraction peaks corresponds to a two-dimensional hexagonal lattice, which is characterized by the relation

$$\frac{1}{d_{hk}} = \frac{\sqrt{4/3 \cdot (h^2 + hk + k^2)}}{a_0}, \qquad (1)$$

where h and k are the Miller indices and $d_{hk} = 2\pi/Q$ is the structure period.

Figure 3 shows the positions and the integrated intensities of Bragg peaks Q_{11}, Q_{20}, and Q_{21} as functions of the annealing temperature in the range 40°C < T < 500°C. The following two temperature ranges of significant changes in the periodicity of the mesoporous matrix can be distinguished: 100–150°C and 230–270°C. The first temperature range corresponds to the

Table 1. Parameters of diffraction peaks and a two-dimensional hexagonal lattice for various samples

Sample	hk	Q, nm^{-1}	d, nm	a_0, nm
Fe–SiO_2–UV	10	1.59(2)	3.95(2)	4.56(2)
	11+20	3.19(2)	1.97(2)	4.55(2)
	21	4.20(2)	1.50(2)	4.57(2)
Fe–SiO_2–260	10	1.70(2)	3.65(2)	4.27(2)
	11+20	3.23(2)	1.95(2)	4.51(2)
	21	4.24(2)	1.45(2)	4.53(2)
Fe–SiO_2–375	10	1.77(2)	3.57(2)	4.12(2)
	11+20	3.45(2)	1.77(2)	4.19(2)
	21	4.57(2)	1.37(2)	4.20(2)

evaporation of physically adsorbed water [19, 20], and we can conclude that the inner surface of the pores in the mesoporous SiO_2 matrix is hydrophobic. The second temperature range is related to the exit of carboxyl groups and elementary carbon, which form as a result of the decomposition of the $Fe(CO)_5$ carbonyl complex under UV radiation along with elementary iron and iron oxides, from the pores.

In diffraction experiments, we did not detect Bragg peaks of the crystalline α-Fe phase or iron oxide (α-Fe_2O_3, γ-Fe_2O_3, Fe_3O_4), which can be associated with a low degree of crystallinity in particles, their imperfection, and their very small sizes. In addition, we note a very high background of the amorphous silicon oxide matrix, which is clearly visible in X-ray diffraction patterns and a rather intense diffuse halo (broad 111 peak of SiO_2) is observed in the Q range where the most intense reflections of iron or iron oxide nanoparticles (from 12 to 30 nm^{-1}) would be expected. The absence of such Bragg reflections was also reported in other works dealing with an investigation of iron or iron oxide nanoparticles at most 5 nm on size embedded in the pores of a silicon dioxide matrix (see, e.g., [21, 22]).

3.3. Mössbauer Spectroscopy

Mössbauer spectroscopy experiments were carried out according to a standard technique in transmission geometry at $T = 4$ and 77 K using a ^{57}Co source on the spectrometer of Delft University of Technology. Samples were placed in plexiglass containers and a 25-μm-thick foil was used for calibration. Figure 4 shows the γ-radiation absorption spectra of the Fe–SiO_2–375 sample at $T =$ (a) 77 and (b) 4.2 K. At $T = 77$ K, the spectrum consists of background scattering and a doublet with an isomer shift $\delta = 0.44 \pm 0.03$ mm/s with respect to α-Fe, a quadrupole splitting $\Delta = 0.92 \pm 0.03$ mm/s, and an absorption line width $\Gamma = 0.69 \pm 0.03$ mm/s. Apart from a quadrupole doublet with the same isomer shift, a smaller quadrupole splitting ($\Delta = 0.85 \pm 0.03$ mm/s), and a larger line width ($\Gamma = 0.82 \pm 0.03$ mm/s), the spectrum at $T = 4.2$ K also has a sextet with an isomer shift $\delta = 0.59 \pm 0.03$ mm/s, a line width $\Gamma = 2.33 \pm 0.03$ mm/s, a hyperfine field $H_{ST} = 47.3$ T, and peak intensity ratios $I_2/I_1 = 1.29$ and $I_3/I_1 = 1.36$.

The following conclusions can be drawn from these spectra. First, the ratio of the peak intensities in the crystalline state (α-Fe) should be $I_2/I_1 = 0.66$ and $I_3/I_1 = 0.33$. The strong deviation from these ratios observed in our spectra demonstrates the presence of a strongly disordered phase subjected to relaxation effects because of the small sizes of iron nanoparticles. Second, the presence of a disordered iron phase inside pores is also supported by the fact that the sextet is only detected at $T = 4.2$ K and a superparamagnetic doublet is detected at $T = 77$ K. Third, if crystalline iron (α-Fe) formed in pores, the iron spectrum for the superparamagnetic state would consist of one line with an isomer shift of about 0.07 mm/s at $T = 4.2$ and 77 K. Moreover, the spectrum of ferromagnetic crystalline iron would consist of a sextet with an isomer shift of 0.07 mm/s and a hyperfine field $H_{ST} = 34$ T.

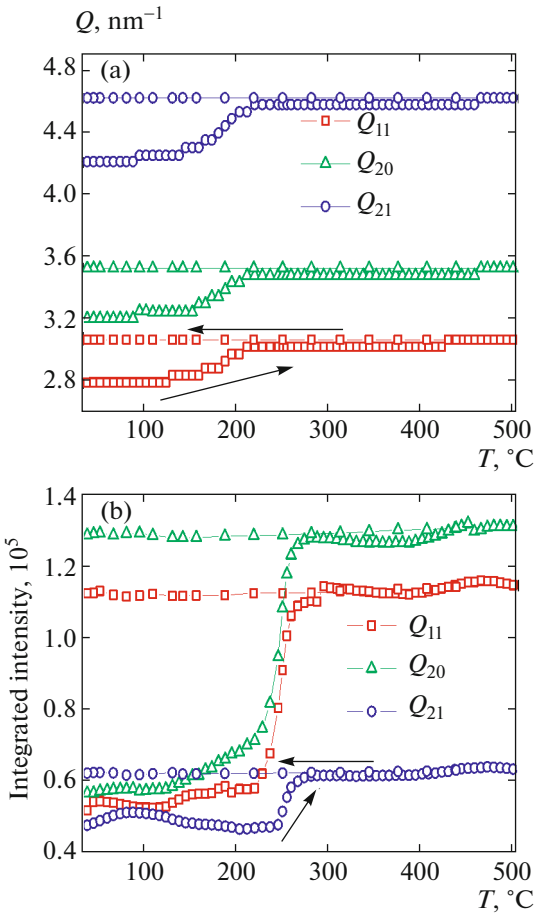

Fig. 3. Temperature dependences of (a) positions and (b) integrated intensities of Bragg reflections Q_{11}, Q_{20}, and Q_{21}.

The authors of [14–16] used Mössbauer spectroscopy to study α-Fe_2O_3 and γ-Fe_2O_3 nanocomposites based on an SiO_2 matrix with various nanoparticle sizes. Samples with a particle size smaller than 8 nm were shown to exhibit superparamagnetic behavior in the temperature range from 300 to 77 K. The spectra of the samples consisted of a paramagnetic doublet with broadened lines, an isomer shift $\delta = 0.28$–0.50 mm/s, and hyperfine field $H_{ST} = 46$–52 T depending on the particle size. As the temperature decreased below 77 K, the samples transformed into a ferromagnetic state (paramagnetic doublet splits into a sextet). The temperature at which the integrated doublet area becomes equal to the integrated sextet area (blocking temperature, when the magnetic anisotropy energy of a particle is comparable with its heat energy) was different for samples with different nanoparticle

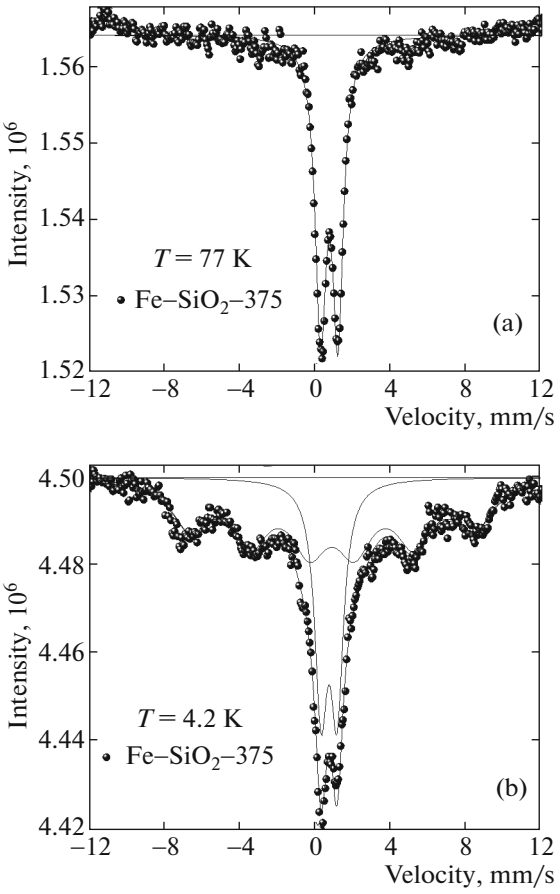

Fig. 4. γ radiation absorption spectra of the Fe–SiO_2–375 sample at $T =$ (a) 77 and (b) 4.2 K.

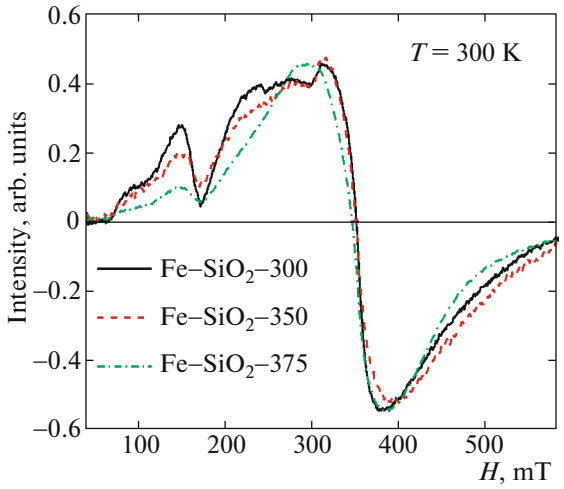

Fig. 5. ESR spectra of the Fe–SiO_2–300, Fe–SiO_2–350, and Fe–SiO_2–375 samples at $T = 300$ K.

sizes. The smaller the nanoparticle size, the lower the blocking temperature. If a sample has a size dispersion of nanoparticles, the blocking temperature extends over a range of 10°–15°, in which the paramagnetic–ferromagnetic transition occurs first in large particles and then in small particles (as temperature decreases). In our measurements, the paramagnetic doublet splits into a sextet only at $T = 4$ K, demonstrating superparamagnetic behavior of the magnetization of nanoparticles in the temperature range 300–77 K. Thus, the thermal fluctuations of the magnetization vector of nanoparticles about 2 nm in diameter are decisive in the orientation of the atom spin as compared to the anisotropy energy or temperature. The contributions of α-Fe_2O_3 and γ-Fe_2O_3 cannot be separated because of the strong broadening of the absorption lines. We can only assume that, as temperature decreases, γ-Fe_2O_3 are more likely to transform into a ferromagnetic state as compared to α-Fe_2O_3 particles, since γ-Fe_2O_3 in the bulk state is a ferromagnet with a magnetic moment of about $430 \times 4\pi \times 10^{-3}$ A m^2/kg and α-Fe_2O_3 in the bulk state is an antiferromagnet with a very low magnetic moment (approximately $1 \times 4\pi \times 10^{-3}$ A m^2/kg). Thus, an analysis of the Mössbauer absorption spectra suggests that iron oxide (α or γ phase) nanoparticles exist in the pores of the silicon dioxide matrix. These nanoparticles are in a superparamagnetic state at $T \geq 77$ K and transform into a ferromagnetic state upon cooling to the liquid-helium temperature. A more detailed investigation of the magnetic state of the samples in the temperature range 77–4 K will be performed in ESR experiments (see Fig. 7 below).

3.4. Electron Paramagnetic Resonance

ESR spectra were recorded on a standard Thomson spectrometer using a closed-cycle Oxford helium cryostat at the Kazan Physical Institute of the Kazan Federal University (Kazan, Russia). The measurements were carried out at temperatures from 4.2 to 500 K and the generation frequency was 9.4 GHz. Figure 5 shows the normalized first derivatives of the ESR spectra of the Fe–SiO_2–300, Fe–SiO_2–350, and Fe–SiO_2–375 samples measured at $T = 300$ K.

As noted in Sections 3.1 and 3.2, the sizes of the nanoparticles containing iron atoms increase with annealing temperature due to their aggregation and the removal of volatile synthesis reaction products from pores. This increase leads to an increase in the exchange interaction in nanoparticles with simultaneous suppression of the dipole–dipole broadening and, hence, a narrowing of the absorption lines with increasing annealing temperature (Fig. 5).

According to [23, 24], the Hamiltonian of free spin ${}^6S_{5/2}$ of trivalent iron Fe^{3+} ions without exchange interaction is written as

$$H = g\beta HS + D\left[S_z^2 - \frac{1}{3}S(S+1)\right] + E(S_x^2 - S_y^2), \quad (2)$$

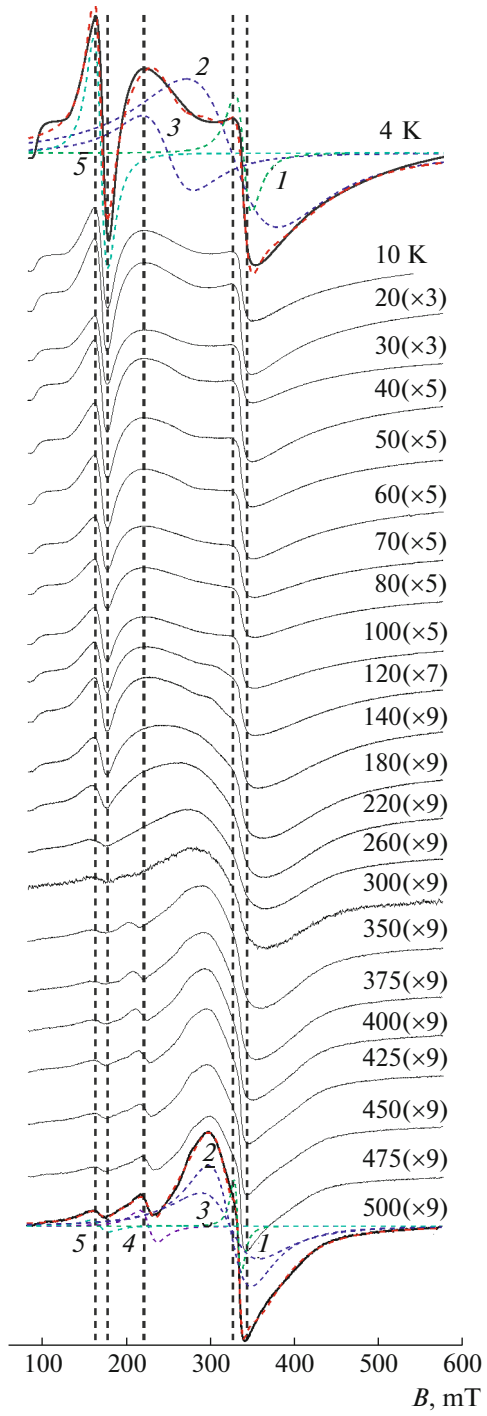

Fig. 6. Temperature dependence of the ESR absorption spectrum of the Fe–SiO_2–375 sample. In parentheses, the ratio of increasing the spectrum intensity with respect to the initial value.

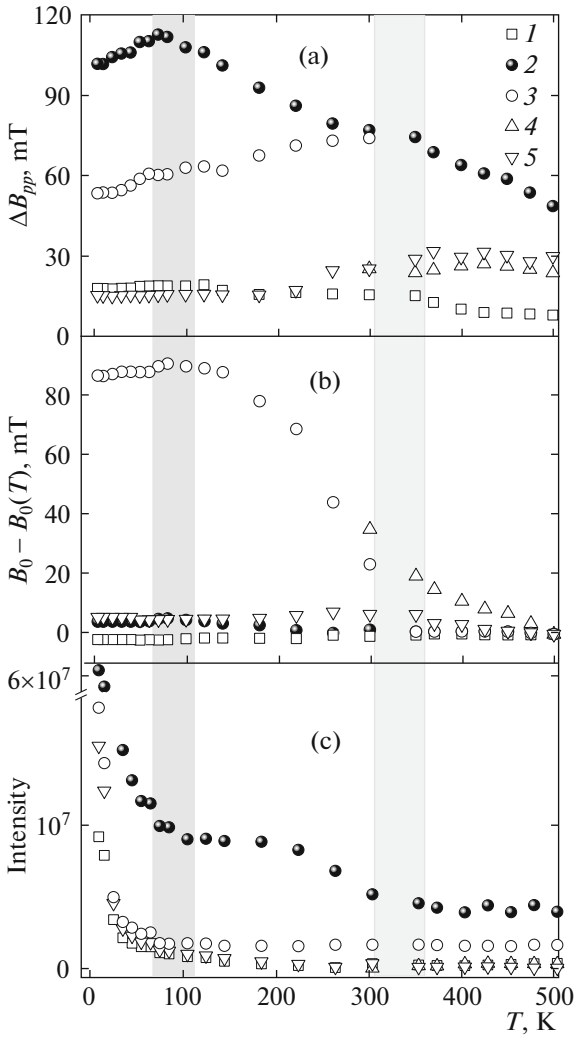

Fig. 7. Temperature dependences of the following parameters of the ESR spectrum approximation using the sum of the first derivatives of five Lorentz functions for the Fe–SiO_2–375 sample: (a) width ΔB_{pp}, (b) shift $B_0 - B_0(T)$, and (c) intensity. The number of the Lorentzians are given in Fig. 6.

where D and E are the gradients of the electric fields with axial and orthorhombic symmetry, respectively. It is well known that the orbital moment of free iron ions is zero, and the ground state is sixfold degenerate and splits into three Kramers doublets $|\pm 1/2\rangle$, $|\pm 3/2\rangle$, $|\pm 5/2\rangle$ in a crystal field. The selection rules allow ESR transitions in doublet $|\pm 1/2\rangle$ with effective values $g = 2.0$ and 6.0 if $D \neq 0$ and $E = 0$ [25]. In the case of $D = 0$ and $E \neq 0$ or a ratio $E/D = 1/3$, a doublet with $g = 2.0$ and 4.29 (last line from Fe^{3+} ions in a low-symmetry surrounding [26]) is observed. If D or E is small, an absorption line of the Fe^{3+} ions located in a symmetric octahedral surrounding will be observed at $g = 2$.

At $T = 300$ K, the absorption curves in Fig. 5 have two groups of asymmetric lines with $g = 4.3$ and 2. This spectrum is characteristic of trivalent iron oxide Fe_2O_3 [27]. The theoretical approximation of the spectra was performed by the method of least squares using the derivative of the sum of five Lorentz functions with respect to H with specific parameters (position, half-width at half-maximum, intensity). As an

example, Fig. 6 shows the temperature dependence of the ESR absorption spectrum of the Fe–SiO_2–375 sample and the results of approximation at $T = 500$ and 4 K. As is seen in Fig. 6, the line with $g \approx 2$ consists of a narrow (line *1*) and two broad components, which split at $T \leq 300$ K (lines *2*, *3*). The intensity of the groups of lines with $g \approx 2$ increases with decreasing temperature. This visual analysis also suggests that the absorption line at $g \approx 4.3$ does not change its position and grows with decreasing temperature (line *5*). The ESR spectrum also contains a resonance line at $g \approx 3.12$ (line *4*).

The approximation parameters are presented in Fig. 7. The absorption line width was taken to be the distance from the maximum to the minimum of its first derivative (peak-to-peak width), and the shift was determined as $B_0 - B_0(T)$, where $B_0(T)$ is the resonance field determined as the point where the absorption derivative equals zero at the temperature T and B_0 is the asymptotic resonance field to which B_0 tends at $T > 400$ K. The error of determining the fitting parameters does not exceed the point sizes in the curves.

The following three temperature ranges should be distinguished in Fig. 7: high-temperature range $300 \text{ K} \leq T \leq 500$ K, medium-temperature range $100 \text{ K} \lesssim T \leq 300$ K, and low-temperature range $4 \text{ K} \leq T \lesssim 100$ K. The most pronounced changes in the temperature dependences of the approximation parameters are detected for lines *2* and *3*, which are caused by the trivalent iron ions located at octahedral and tetrahedral sites. They exhibit the typical temperature behavior of many magnetic nanoparticles (e.g., Cu–Co, α-Fe_2O_3, γ-Fe_2O_3, FeOOH, ferritic particles) embedded in diamagnetic matrices (SiO_2, Al_2O_3, polyethylene, other polymer matrices) [28–32]. The behavior of lines *2* and *3* in the high-temperature range is similar: their positions and intensities almost do not change, and the line width decreases identically with decreasing temperature. In the central temperature range, line *2* continues to broaden significantly when temperature decreases to $T \approx 100$ K, shifts weakly toward the low-field part of the spectrum, and grows almost twofold in intensity. In the temperature range $100 \text{ K} \lesssim T \leq 300$ K, line *3*, in contrast, tends to narrow with decreasing temperature and to shift noticeably toward low magnetic fields at an almost constant intensity. The decrease in the ESR line width with increasing temperature is related to the transition of the nanoparticles into a paramagnetic state (Fig. 7a). The magnetic particles in macroscopically isotropic systems are randomly oriented. An applied magnetic field or the shape anisotropy of particles orients the magnetic moments of nanoparticles along a certain direction; however, thermal fluctuations return the system to a disordered state. As a result, we can see a paramagnetic narrowing of the resonance spectrum at high temperatures or a broadening of the spectrum at low temperatures because of the dipole–dipole interaction of particles. However, the widths of lines *2* and *3* in the low-temperature range $4 \text{ K} \leq T \lesssim 100$ K tend to decrease, their positions do not change, and their intensities grow significantly (Fig. 7).

An absorption line at $g \approx 3.12$ (line *4*) is clearly visible in Fig. 7 in the temperature range $300 \text{ K} \leq T \leq 500$ K. This line shifts toward low fields with decreasing temperature at the rate that is identical to that of line *3* (Fig. 7b). Then, intersecting with line *5*, it goes outside of the available range of variation of the external magnetic field. An analysis of the temperature dependence of the ESR spectrum parameters for lines *2*, *3*, and *4* demonstrates that two magnetic subsystems of iron atoms, which are located in crystal field of different symmetries, can coexist. The first subsystem is described by absorption line *2*, and the second subsystem is described by lines *3* and *4*, which correspond to the transverse and longitudinal components of the *g* factor, respectively. The existence of two subsystems can be related to, first, the geometric anisotropy of a nanoparticle. As was shown in the micrographs in Fig. 1, the particles form inside cylindrical pores with an aspect ratio of several tens of units. Second, the existence of the two subsystems can be associated with surface effects, where the gradients of the electric crystal field are different in the particle volume and on the particle surface because of broken chemical bonds [31, 33].

Thus, the temperature dependences of the fitting Lorentzian parameters point to the existence of two characteristic temperatures near 300 and 100 K (Fig. 7). At $T \approx 300$ K, the width of line *3* passes through a maximum (Fig. 7a), the intensity of line *2* grows sharply (Fig. 7c), and the shift $B_0 - B_0(T)$ of line *3* increases strongly (Fig. 7b). This behavior can be explained by the lattice distortions induced by the Morin transition in α-Fe_2O_3 nanoclusters from an antiferromagnetic state with fully compensated spins into a weak ferromagnetic state with incomplete compensation of magnetic moments. At $T \approx 100$ K, the width of line *2* passes through a maximum (Fig. 7a); the second sharp increase in the line *2* intensity is observed; a sharp increase in the intensities of lines *1*, *3*, and *5* takes place (Fig. 7c); and the position of line *3* is stabilized and remains unchanged with decreasing temperature (Fig. 7b). Note that this temperature coincides with the temperature of the maximum specific magnetic susceptibility measured in an applied magnetic field $h_a = 10$ mT when temperature increases from 4 to 300 K (Fig. 8c).

Narrow line *1* at $g \approx 2$ is clearly visible at low temperatures (from 4 to 140 K). The *g* factor of this narrow line remains unchanged ($g = 2.0020 \pm 0.0004$) when temperature changes. This line is assumed to be caused by ferromagnetic pure iron clusters.

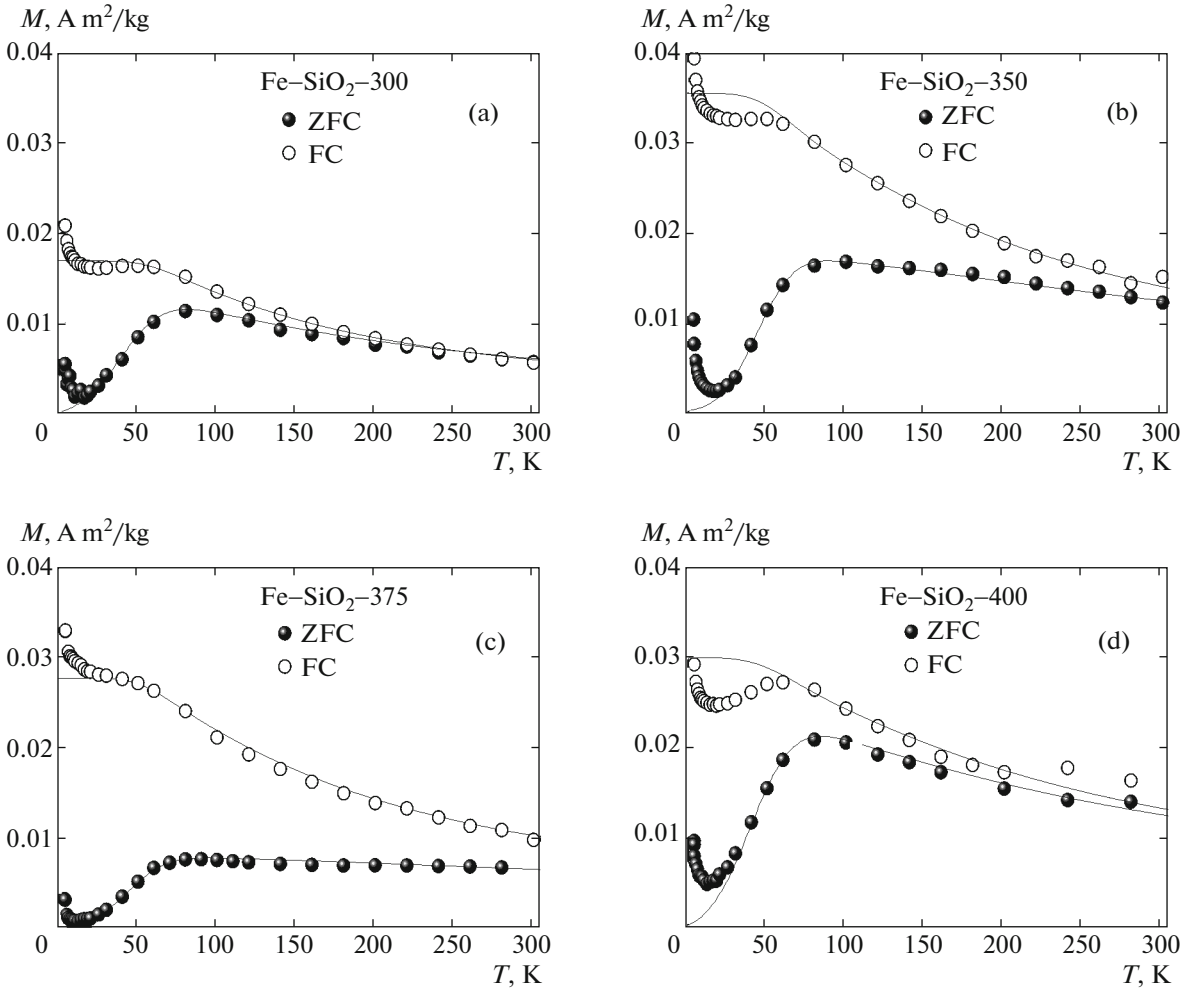

Fig. 8. Temperature dependences of the specific magnetizations of the composites (a) Fe–SiO_2–300, (b) Fe–SiO_2–350, (c) Fe–SiO_2–375, and (d) Fe–SiO_2–400 (points) and (solid lines) curves calculated in terms of the Preisach model for ZFC and FC processes at $h_a = 10$ mT.

Line *5* at $g \approx 4.3$ corresponds to the trivalent iron atoms located in strongly deformed orthorhombic sites. This absorption line is most likely to be generated by the iron atoms that partly substitute for silicon atoms in oxygen tetrahedra in the inner pore surfaces and by the iron atoms that are located on the nanoparticle surfaces. The line position and width are most likely to remain unchanged when temperature changes and are $g = 4.281 \pm 0.002$ and $\Delta B_{pp} = 0.028 \pm 0.001$ T, respectively. (The insignificant changes in these parameters of lines *1* and *5* in the high-temperature range in Fig. 7 should be attributed to the difficulty of their determination in low-resolution spectra.)

Thus, we can conclude that the nanoparticles synthesized in the pores of the silicon dioxide matrix consist of trivalent iron oxide (α-Fe_2O_3, γ-Fe_2O_3) clusters and clusters of several exchange-coupled iron ions.

4. MAGNETIC PROPERTIES OF THE NANOCOMPOSITE MATERIALS BASED ON A MESOPOROUS SILICON DIOXIDE MATRIX

4.1. SQUID Measurements

To study the integral magnetic properties of the nanocomposites, we measured the temperature and field dependences of magnetization at $T = 4$–300 K and $0 < H \le 1$ T. The measurements were carried out on an S600 superconducting quantum interference APD cryogenics device (SQUID magnetometer). ZFC (zero field cooling) magnetization curves were recorded after the following two manipulations with an applied field and temperature: (i) when samples were cooled from 300 to 4 K in a magnetic field $H = 0$; (ii) a positive dc magnetic field $h_a = 10$ mT was applied and the magnetization was measured when temperature increased from 4 to 300 K. Thus, it is correctly to call this procedure FH (field heating) after ZFC. Nev-

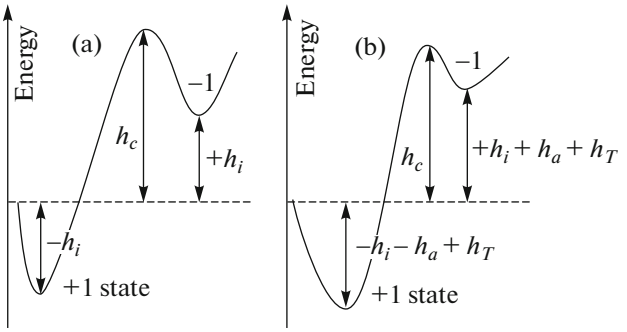

Fig. 9. Diagrams of the energy levels with two local minima separated by energy barriers (a) $h_c - h_i$ and $h_c + h_i$ and (b) $h_c - h_i - h_a + h_T$ and $h_c + h_i + h_a + h_T$.

ertheless, we will call this procedure ZFC assuming that this comment is sufficient. When the sample was then cooled to 4 K in the presence of a magnetic field (h_a = 10 mT), an FC (field cooling) curve was recorded. Figure 8 shows the temperature dependences of the magnetization $M(T)$ of the nanocomposites Fe–SiO_2–300, Fe–SiO_2–350, Fe–SiO_2–375, and Fe–SiO_2–400 during the ZFC and FC processes.

In a macroscopically isotropic system, the magnetic anisotropy axes of nanoparticles remain randomly oriented in the ZFC process. The magnetization measured in heating of a sample in a low magnetic field after ZFC exhibits an initial increase in the specific magnetization to a certain temperature and, then, a decrease. In the FC process, magnetization vectors are mainly oriented along the magnetic field vector; that is, the magnetization increases with decreasing temperature [28, 34, 35]. As is seen in Fig. 8, the ZFC curves of the Fe–SiO_2–300, Fe–SiO_2–350, Fe–SiO_2–375, and Fe–SiO_2–400 samples have maxima at different temperatures. The recorded $M(T)$ dependences are satisfactorily described in terms of the well-known Preisach model [36], which takes into account the anisotropy of a particle and the interparticle interaction. This model can be used to calculate the magnetic moment of the system at an arbitrary sequence of application and removal of a magnetic field.

According to the Preisach model, all magnetic systems are divided into a large set of two-level subsystems. Each subsystem is characterized by two states, which correspond to two discrete magnetic-moment orientations, and two critical unstable fields, namely, coercive field h_c, which operates as the intrinsic anisotropy field, and asymmetric field h_i, which plays the role of the local field of interaction of two neighboring subsystems (Fig. 9). When the subsystems are cooled in a zero magnetic field to $T = 0$ K, all magnetic moments are in equiprobable states +1 and −1, and the average magnetization of the entire system is zero (Fig. 9a). To induce transitions between two energy levels, either magnetic field h_a or temperature (thermal field h_T) should be applied to the subsystems. Applied magnetic field h_a stabilizes state +1 and destabilizes state −1, and h_T always exerts a destabilizing effect on both states +1 and −1 (Fig. 9b). In particular, each system upon heating in a zero magnetic field ($h_a = 0$) after cooling (ZFC) passes through characteristic temperature T_B (blocking temperature) at which h_T is equal to the energy of the potential barrier that is maximal among two barriers. At this temperature, thermal fluctuations exhaust the highest metastable energy level (state −1 in Fig. 9b with $h_a = 0$), and the subsystems pass to the lowest stable energy level (state +1).

In this case, the subsystem blocking temperature is

$$T_B = \frac{h_c + |h_i|}{k_B \ln(t/\tau)}, \quad (3)$$

where k_B is the Boltzmann constant and $\ln(t/\tau)$ is the time-dependent parameter with a standard measurement time $t \sim 10^2$–10^3 s; we assume that the system under study returns to the unexcited state in time $\tau \sim 10^{-9}$ s. At $T > T_B$, the system transforms into a paramagnetic state with a decreased average magnetization because of thermal instability and constant reorientation of the magnetic moments of the subsystems. This state of the system is characterized by thermal equilibrium (probability of existing the system between level +1 ($\exp(h_i/k_BT)$) and level −1 ($\exp(-h_i/k_BT)$))

$$\frac{\exp(h_i/k_BT) - \exp(-(h_i/k_BT))}{\exp(h_i/k_BT) + \exp(-(h_i/k_BT))} = \tanh\left(\frac{h_i}{k_BT}\right). \quad (4)$$

If the system is heated from 0 K to temperature $T > T_B$ in a positive dc magnetic field $h_a > 0$, the blocking temperature shifts toward low temperatures (Fig. 9b, $h_a > 0$), and the magnetic moment of each subsystem is proportional to $\tanh((h_a - h_i)/k_BT)$. The magnetic moment of the entire system is written as the sum of the moments of the subsystems with the weight Preisach function

$$p(h_c, h_i) = \frac{\exp((h_c - \overline{h}_c)^2/2\sigma_c^2)}{\sqrt{2\pi\sigma_c^2}} \frac{\exp(h_i^2/2\sigma_i^2)}{\sqrt{2\pi\sigma_i^2}}, \quad (5)$$

where σ_i is the mean deviation of the interaction between particles h_i, the mean is $\overline{h}_i = 0$ because of random variations of the nearest surrounding, σ_c is the mean deviation of coercive field h_c, and $\overline{h}_c$ is the mean value of h_c. Thus, the magnetization of the system is

$$M = \int_{-\infty}^{\infty} dh_i \int_0^{\infty} \phi(h_c, h_i) p(h_c, h_i) dh_c. \quad (6)$$

All field parameters (σ_i, σ_c, h_T) were normalized by the mean coercive field; therefore, we have $\overline{h}_c = 1$. The results of Preisach approximation of the experimental specific magnetization curves are presented in Fig. 8 and Table 2.

Table 2. Parameters of the Preisach approximation of the magnetization curves

Sample	Measurement mode	σ_c, mT	σ_i, mT
Fe–SiO_2–300	ZFC	50	9
	FC	50	1
Fe–SiO_2–350	ZFC	35	25
	FC	35	5
Fe–SiO_2–375	ZFC	35	25
	FC	35	5
Fe–SiO_2–400	ZFC	50	12
	FC	50	9

The applied magnetic field was the same for all samples (h_a = 10 mT), and mean coercive field was $\overline{h_c}$ = 100 mT. The mean deviation of the coercive field was smaller for the samples annealed at T = 350 and 375°C, which is related to the maximum anisotropy parameter of magnetic nanoparticles in these samples and agrees well with the TEM data (Fig. 1) and the measured magnetization reversal curves (Table 3). In turn, interparticle interaction fluctuations σ_i are on the order of the effective field (11 mT) determined from the field dependence of the position of the maximum in the ZFC $M(T)$ curve (Fig. 10). The different values of σ_i in the ZFC and FC measurements of the same sample are most likely to be associated with the relaxation of the magnetization vector. The field dependence of the maximum (T_{max}) in the ZFC curves in Fig. 10 has two specific features. The first specific feature is the inflection point at $h_a \approx 11$ mT, which means that the effective magnetic field on a certain filament from other nanofilaments becomes negligibly small as compared to the increasing applied magnetic field ($h_a \gg h_i > h_c$). Indeed, blocking temperature T_B at low applied fields (weak field mode) changes insignificantly, which demonstrates that the interfilament interaction is higher than the interaction between a filament and an applied magnetic field. At high magnetic fields, T_B decreases sharply and indicates a strong field mode, where the interfilament interaction is lower than the interaction between a filament and an applied magnetic field. The second specific feature is the intersection of the curve with the abscissa at $T \approx$ 80–90 K. This finding means that the nanocomposite under study undergoes the paramagnetic–ferromagnetic phase transition when temperature decreases ($h_a \ll h_i$, $h_a \ll h_c$).

Let us make some notes, which are important from both theoretical and practical standpoints. First, the temperatures of the maxima in the ZFC $M(T)$ curves are not the blocking temperature (Fig. 8). According to the calculations using the Preisach model, blocking in our experiments occurs at a temperature $T_B \approx$ 22.5 K, where the activation thermal energy becomes comparable with or higher than the energy barrier (Fig. 9b). The ZFC maxima in the low-temperature segment of the $M(T)$ dependence lie significantly higher than this blocking temperature. The blocking temperature is thought to be the inflection point in the $M(T)$ dependence, where the rate of change of magnetization dM/dT is maximal. In other words, for low applied magnetic fields ($h_a \ll h_c$), the change in dM/dT is maximal at $h_a + h_T = h_c$, which is the blocking condition $k_B T_B \approx h_c/\ln(t/\tau)$ [37].

Second, it is necessary to discuss the coercive force in detail, since it is proportional to the applied magnetic field required to decrease the magnetization of the material to zero. On the one hand, a high coercive force allows more reliable data storage and makes it possible to avoid spontaneous magnetization reversal when storage conditions (temperature, pressure, humidity) change. On the hand, a low coercive force can be used to remove old information completely and to record new information clearly. Thus, conflicting requirements are imposed on magnetic data storage systems. At present, the coercivity boundaries of magnetic data recording and storage devices are from 30 mT (low-energy devices) to 400 mT (high-energy devices). The magnetization reversal of a single-domain magnetic particle from a certain direction of its magnetization vector to the opposite direction needs the applied magnetic field that is higher than the energy barrier (Fig. 9b). Magnetization reversal depends on the applied magnetic field amplitude, the

Table 3. Magnetic parameters of the nanocomposites

Sample	T_{max}, K	L/D	h_c, mT		$M_s \times 4\pi \times 10^{-3}$, A m^2/kg
			4 K	300 K	300 K
Fe–SiO_2–260	76 ± 3	16 ± 2	22.0 ± 0.1	2.0 ± 0.2	0.25 ± 0.03
Fe–SiO_2–300	80 ± 3	20 ± 2	40.0 ± 0.1	18.0 ± 0.2	0.32 ± 0.03
Fe–SiO_2–350	87 ± 3	32 ± 2	46.0 ± 0.1	20.0 ± 0.2	0.53 ± 0.03
Fe–SiO_2–375	84 ± 3	45 ± 2	54.0 ± 0.1	22.0 ± 0.2	0.61 ± 0.03
Fe–SiO_2–400	84 ± 3	35 ± 2	53.0 ± 0.1	19.0 ± 0.2	0.76 ± 0.03

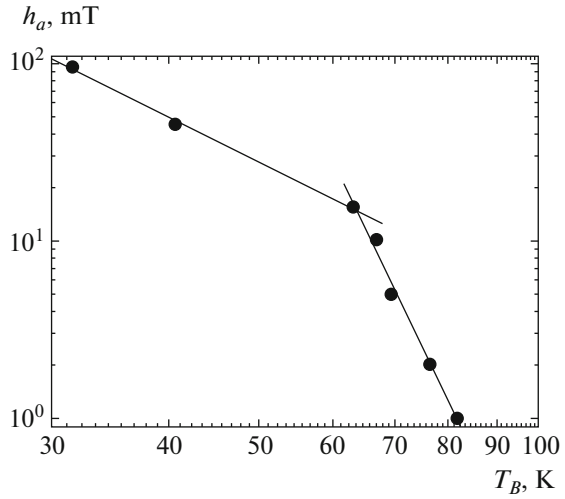

Fig. 10. Field dependence of the position of the maximum in the ZFC $M(T)$ dependence of the Fe–SiO_2–375 sample.

time of field action, and the particle shape. Using the Stoner–Wohlfarth theory [38], we can more correctly estimate coercive field h_c, which acts as the intrinsic anisotropy field. If magnetic field h_a is applied along the easy magnetization axis of a subsystem, the energy barrier induced by the intrinsic anisotropy of the subsystem changes with h_a as $E_a = (h_c/2)[1 + (h_a/h_c)^2]$; that is, it grows from the minimum value $E_a = h_c/2$ to the maximum value $E_a = h_c$. Thus, the Preisach model overestimates the thermal activation barrier when h_a has a near-critical value, so that the instability criteria based on the energy diagram in Fig. 9b underestimate the efficiency of thermal fluctuations in inducing phase transitions. This finding explains why σ_i from Table 2 coincides with the effective magnetic field determined from Fig. 10 only in an order of magnitude.

Third, we have to reveal the nature of interaction h_i between the subsystems. As noted above, our system consists of cylindrical 2 × 100 nm pores arranged in a regular hexagonal manner. Nanoparticles with the sizes that are comparable with the pore sizes are inside the pores. The average magnetic moment of each nanoparticle $\langle\mu\rangle$ interacts with other average moments of neighboring nanoparticles through a magnetic dipole–dipole interaction with the energy

$$h_i = E_{ij} = \frac{\langle\mu_i\rangle\langle\mu_j\rangle(1 - 3\cos^2\Theta_{ij})}{r_{ij}^3}. \qquad (7)$$

The crystal field inside each nanoparticle creates an easy magnetization axis with average magnetic moment $\langle\mu\rangle$. Each easy axis is frozen and randomly oriented in an applied magnetic field at temperatures lower than certain critical point T_{max}. Upon heating, the interparticle interaction energy increases and the average magnetic moment of the entire system increases to a certain critical value. Depending on the magnetization of the subsystem (degree of crystallization or homogeneity of nanoparticles), the characteristic point of interparticle interaction changes its position in the temperature scale. The higher the magnetization, the larger the shift toward high temperatures ($T_{max} > T_B$). Depending on the orientations of the magnetization vectors of the subsystems with respect to each other, the dipole–dipole interaction turns out to be ferromagnetic for the particles located in one pore and to be antiferromagnetic for the particles located in neighboring pores. The system under study can exhibit dipole-glass behavior at low temperatures ($T < T_{max}$), where magnetization vectors are frozen in an arbitrary order, or in the case of a diluted magnetic system, where the interparticle distances are larger than the radius of action of the dipole interaction forces.

As is seen from Table 3, the characteristic point of the maximum in the temperature dependence of magnetization $M(T)$ (second column) shifts toward high temperatures as the annealing temperature increases. In other words, the dipole interaction between the nanoparticles embedded into the diamagnetic silicon matrix increases with the annealing temperature. The temperature of the maximum T_{max} determined experimentally for the Fe–SiO_2–375 sample (see Fig. 10) differs from the blocking temperature of the system T_B because of the contribution of the magnetic dipole interaction between nanofilaments.

Fourth, an increase in the specific magnetization at $T \le 20$ K is clearly visible in Fig. 9. This behavior of magnetization correlates with the sharp change in the intensities of the resonance lines in the ESR spectra in Fig. 7c and corresponds to the transition of the nanoparticles into a superparamagnetic state.

To determine the saturation magnetization (M_s) and the coercive force of the nanoparticles, we measured magnetization reversal curves for all samples at $T = 4$ and 300 K. The typical hysteretic $M(H)$ dependences of the Fe–SiO_2–375 sample are shown in Fig. 11. The data in Table 3 demonstrate an increase in the coercive force with the annealing temperature, which is related to an increase in the homogeneity and size of the magnetic nanowires inside pores (as was noted above).

4.2. Small-Angle Polarized-Neutron Scattering

SAPNS experiments were carried out on the SANS-2 installation of the research FRG-1 reactor in Geesthacht, Germany. The schematic diagram of the experiments is shown in Fig. 12. We used a polarized neutron beam with a polarization $P_0 = 0.96$, a wavelength $\lambda = 0.58$ nm ($\Delta\lambda/\lambda = 0.01$) and a divergence of 1.5 mrad. The sample–detector distance was 1 m, and the momentum-transfer range was 0.1–2 nm^{-1}. In the case of the powder Fe–SiO_2–T, Fe–SiO_2–UV, and SiO_2 (mesoporous matrix) samples, the neutron dif-

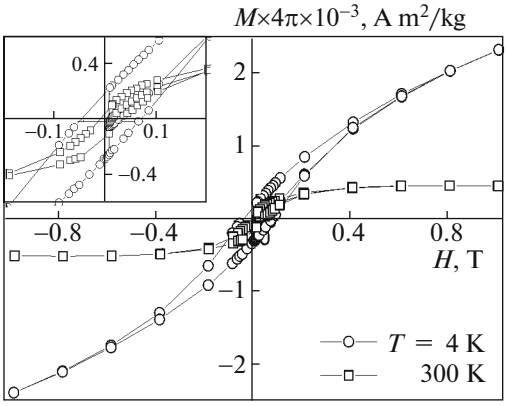

Fig. 11. Magnetization reversal curves of the Fe–SiO_2–375 sample at $T = 300$ K and $T = 4$ K.

fraction patterns consist of concentric rings, which mainly result from scattering by pores or embedded nanofilaments located parallel to the incident neutron beam (inset to Fig. 13). This is related to the fact that the coherent volume of neutron scattered by the small angles is effectively extended along the beam and the coherent volume of nanofilaments (nanopores) is extended along a filament (pore). If the axis of filaments (pores) coincides with the beam axis, the scattering efficiency increases by many times (see, e.g., [39]). To study the field dependence of the neutron scattering intensity, we applied a magnetic field H = 0–350 mT (forward run) and H = 350–0 mT (backward run) in the horizontal plane normal to the incident beam. The sample temperature was changed from 10 to 300 K with an accuracy of 0.5 K. The neutron scattering cross section is determined by Eq. (8) and includes the components of nuclear scattering (Eq. (9)), magnetic scattering (Eq. (10)), and nuclear–magnetic interference (Eq. (11)). The total (nuclear and magnetic) neutron scattering was experimentally determined as the sum

$$I(Q) = \frac{1}{2}(I(Q,+P_0) + I(Q,-P_0)),$$

and neutron-polarization-dependent scattering was determined as the difference

$$\Delta I(Q) = \frac{1}{2}(I(Q,+P_0) - I(Q,-P_0))$$

between the scattering of neutrons polarized parallel $I(Q, +P_0)$ and antiparallel $I(Q, -P_0)$ to an applied magnetic field,

$$I_{\text{tot}} = I_{\text{nuc}} + I_{\text{mag}} + I_{\text{int}}, \quad (8)$$

where

$$I_{\text{nuc}} \propto |A_n S(\mathbf{Q})F(Q)|^2, \quad (9)$$

$$I_{\text{mag}} \propto |A_m \mathbf{m}_{\perp Q} S(\mathbf{Q})F(Q)|^2, \quad (10)$$

$$I_{\text{int}} \propto (2\mathbf{P}_0\langle\mathbf{m}\rangle_{\perp Q})A_n A_m |S(\mathbf{Q})F(Q)|^2. \quad (11)$$

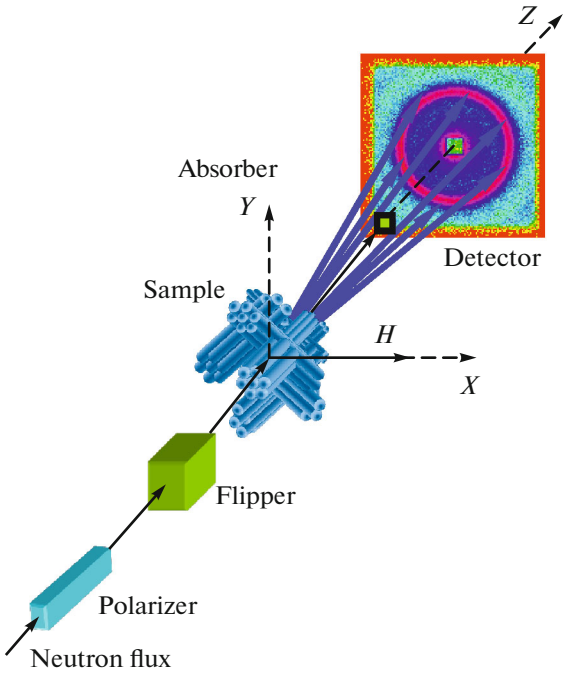

Fig. 12. SAPNS experiments.

Figure 13 shows the neutron scattering intensity as a function of the momentum-transfer $I(Q)$ for the Fe–SiO_2–UV, Fe–SiO_2–300, and Fe–SiO_2–375 samples. It is seen that the introduction of iron oxide nanoparticles in silicon matrix pores leads to an increase in the diffraction peak intensity ($Q \approx 1.6$ nm^{-1}) and a small shift toward high Q. This means that the filling of matrix pores with iron pentacarbonyl, ultraviolet irradiation, and annealing of the samples do not break the matrix: it only insignificantly changes the lattice parameter of the two-dimensional hexagonal lattice from $a_0 = 4.71 \pm 0.02$ to 4.45 ± 0.02 nm. The results of determining a_0 by SAPNS and synchrotron radiation diffraction agree well with each other (Table 1). In the range 0.1 nm^{-1} < Q < 0.5 nm^{-1}, the neutron scattering intensity increases for the annealed samples in comparison with Fe–SiO_2–UV, and the diffuse scattering decreases significantly (which is clearly visible in the range 0.5 nm^{-1} < Q < 2.5 nm^{-1}). The decrease in the diffuse scattering is related to the exit of the hydrogen-containing volatile components of the template and iron pentacarbonyl in annealing process.

The intensity of neutron scattering by spatially ordered powder nanosystems consists of the following three contributions: scattering by micron-sized powder particles, scattering by a regular pore structure, and scattering by individual nanowires or nanotubes [40]. The last contribution to scattering can be represented as scattering by cylinders of length L and radius R. This scattering can be presented by the equation

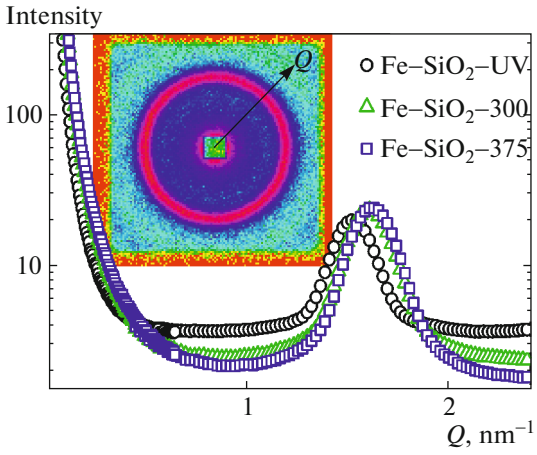

Fig. 13. Q dependences of the total scattering $I(Q)$ of the Fe–SiO_2–UV, Fe–SiO_2–300, and Fe–SiO_2–375 samples at $H = 300$ mT. (inset) Two-dimensional scattering map of a powdered Fe–SiO_2–T sample.

$$F(Q) = \int_0^{\pi/2} \left(\frac{\sin\left(\frac{QL}{2}\cos(\theta)\right)}{\frac{QL}{2}\cos(\theta)} \frac{2J_1(QR\sin(\theta))}{QR\sin(\theta)} \right) \sin(\theta) d\theta, \quad (12)$$

where $2J_1(QR\sin(\theta))$ is the Bessel function of the first kind and θ is the angle between the cylinder axis and Q. If $QL \gg 1$ ($Q > 0.1$ nm^{-1} and $L > 50$ nm), Eq. (12) is simplified taking into account the fact that

$$\frac{\sin\left(\frac{QL}{2}\cos(\theta)\right)}{\frac{QL}{2}\cos(\theta)} \to \delta\left(\theta - \frac{\pi}{2}\right).$$

Thus, the form factor is rewritten as

$$F(Q) \approx \left[\frac{2J_1(QR\sin(\theta))}{RQ} \right]^2$$

and the scattering intensity is

$$I(Q) = A_1 \frac{1}{Q^4} + A_2 \exp\left(-\frac{(Q - Q_c)^2}{2\omega^2} \right) + A_3 \int \left[\frac{2J_1(QR\sin(\theta))}{QR} \right]^2 \times \exp\left(-\frac{(R - R_b)^2}{2\Delta R^2} \right) dR + I_{bg}. \quad (13)$$

The first term in Eq. (13) describes scattering by micron-sized powder particles (Porod approximation). The second term, namely, the diffraction peak with center at Q_c and width ω describes scattering by the structure of a regular pore or nanowire (cylindrical nanoparticle). The third term describes the additional scattering that appears in the samples with pores filled with magnetic nanoparticles for the case at $Q > 0.1$ nm^{-1} and $L > 50$ nm. The last term I_{bg} describes the diffuse scattering related to experimental conditions. In general, the experimental curves are well described by the sum of the contributions of the four types of scattering (Eq. (13)). The approximation of the experimental data demonstrates that the increase in the neutron scattering intensity at small Q (0.1 nm$^{-1} < Q < 0.5$ nm^{-1}) for the annealed samples is associated with scattering by aggregates of radius $R_b = 4.68$ nm with a distribution $\Delta R = 0.9$ nm for the Fe–SiO_2–375 and Fe–SiO_2–400 samples and with scattering by aggregates of radius $R_b \approx 11.0$ nm with small distribution $\Delta R = 4.2$ nm for the Fe–SiO_2–300 and Fe–SiO_2–350 samples. Thus, the samples exhibit nonuniform filling of pores with magnetic nanoparticles in the sample volume.

Information on the magnetic subsystem of a sample can be obtained from, first, the $I(Q)$ curves measured at various applied magnetic fields and temperatures, $\Delta I_H(Q) = I(Q, H) - I(Q, 0)$ and $\Delta I_T(Q) = I(Q, T) - I(Q, 300)$. Here, the scattering intensity is proportional to the magnetic moment of the sample squared (Eq. (10)). Second, this information can be obtained from an analysis of the polarization-dependent part of scattering, which is caused by the interference of the nuclear and magnetic contributions. In this case, the scattering intensity is proportional to the average projection of the magnetic moment vector of a sample onto the magnetic field direction (Eq. (11)).

Figure 14 shows the typical Q dependences of the magnetic contribution to the neutron scattering, $\Delta I_H(Q)$ at $T = 300$ K and $\Delta I(Q)$ at $H = 0$. These curves have two clear contributions, namely, small-angle scattering by aggregates of radius R_b and small-angle diffraction (Bragg peak) by a regular system of magnetic nanofilaments. The position of the diffraction magnetic peak coincides with the maximum of the nuclear scattering cross section at momentum-transfer $Q = 1.65$ nm^{-1}. The $\Delta I_H(Q)$ dependence is the difference between the magnetic cross sections of a sample in the following two states: the fully demagnetized state at $H = 0$ and the magnetized state at $H \neq 0$.

The temperature dependence of the total intensity of small-angle neutron diffraction in the region of the diffraction peak of the Fe–SiO_2–375 sample is shown in Fig. 15a for zero-field heating and cooling in a field $H = 300$ mT. These data agree satisfactorily with the ESR and SQUID magnetometry data (Section 3.4, Fig. 7; Section 4.1, Fig. 8), which demonstrate that thermal fluctuations begin to play a key role at $T \geq 50$–60 K in a field $H = 0$ and at $T \approx 80$ K in a field $H = 300$ mT. As a result, the ferromagnetic state of the system transforms into the paramagnetic state.

In all cases, interference contribution $\Delta I(q)$ to the Bragg reflection for the Fe/SiO_2–T samples turned out to be statistically unresolved. Figure 15b shows the

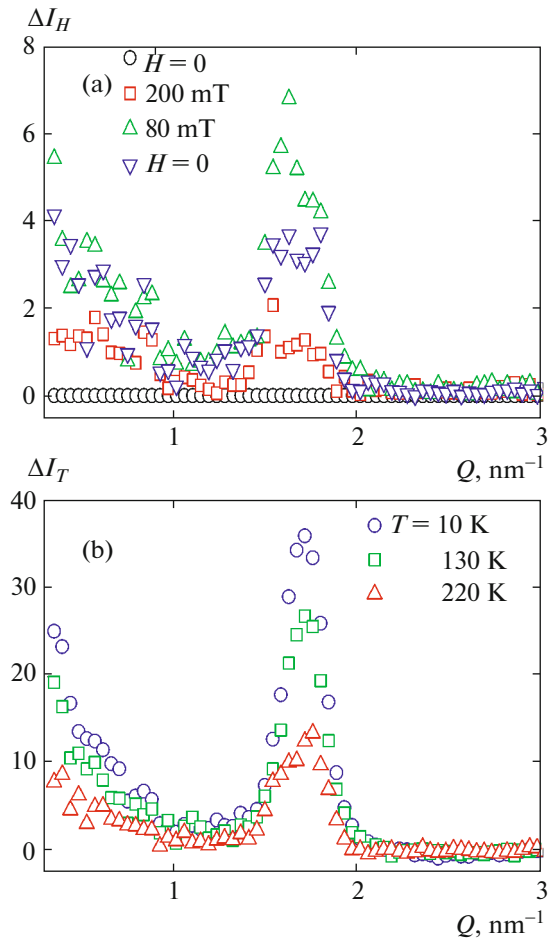

Fig. 14. Q dependence of the magnetization contribution to the neutron scattering that is calculated as the difference between (a) the total scattering intensities in field $H \neq 0$ and zero field $H = 0$ ($\Delta I_H(Q) = I(Q, H) - I(Q, 0)$) at $T =$ 300 K and (b) the total scattering intensities at $T \neq 300$ K and $T = 300$ K ($\Delta I_T(Q) = I(Q, T) - I(Q, 300)$) at $H = 0$ for the Fe–SiO_2–375 sample. Circles and squares in (a) correspond to forward run, while triangles correspond to backward run.

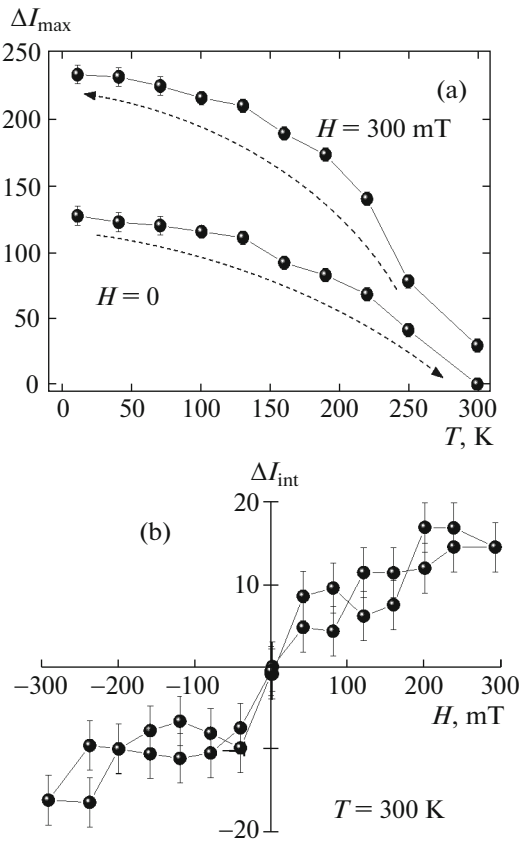

Fig. 15. (a) Temperature dependences of the integrated ZFC and FC ($H = 300$ mT) small-angle neutron diffraction intensities for the Fe–SiO_2–375 sample. (b) Field dependence of the integrated intensity of interference contribution ΔI in the transferred momentum range 0.1 $nm^{-1} < Q < 0.5$ nm^{-1} at $T = 300$ K.

field dependence of the total intensity of the interference contribution for low Q (0.1 $nm^{-1} < Q < 0.5$ nm^{-1}). Since the interference contribution intensity is proportional to the projection of the magnetization vector on the direction of the applied magnetic field, these data coincide satisfactorily with the magnetization reversal curves measured by SQUID magnetometry (Fig. 11).

The field dependences of the total intensity of neutron scattering in the position of Bragg peak I_B for $Q =$ 1.65 nm^{-1} and $T = 300$ and 10 K are shown in Fig. 16 in the range from –300 to +300 mT for the Fe–SiO_2–375 sample. It is seen that the behavior of the magnetic reflection intensity during magnetization reversal at high ($T = 300$ K) and low ($T = 10$ K) temperatures is the same. Specifically, as the applied magnetic field increases during magnetization reversal, the reflection intensity first decreases at $|H| < 100$ mT and then increases up to the reversal point at $H = 300$ mT. As the applied magnetic field decreases, the reflection intensity increases sharply at $|H| > 100$ mT and then decreases to the initial value when the field approaches zero. In [41], we comprehensively analyzed the H dependence of the magnetic contribution into the neutron scattering by an array of ordered magnetic nanofilaments embedded in a diamagnetic matrix and showed that this behavior of the magnetic contribution intensity during magnetization reversal was caused by the magnetostatic interaction between nanofilaments at the fields that were lower than the saturation field. In that work, we also proposed a theory to describe the magnetic properties of the arrays of interacting ferromagnetic nanofilaments in a magnetic field.

5. CONCLUSIONS

The structural and magnetic properties of the nanocomposite materials based on a chemically inert diamagnetic silicon dioxide matrix were studied using

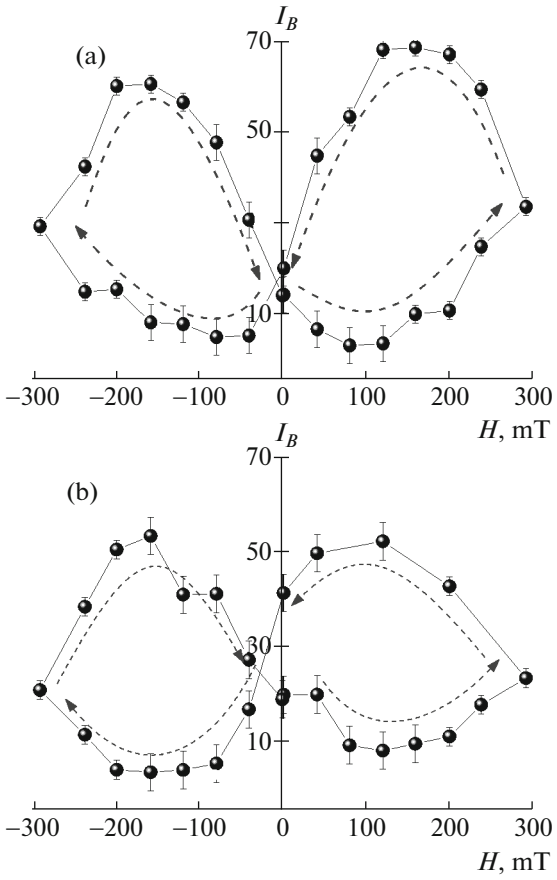

Fig. 16. Integrated small-angle neutron diffraction intensity vs. magnetic field at (a) $T = 300$ and (b) 10 K for the Fe–SiO_2–375 sample.

a large set of mutually complementary experimental techniques. The synthesized nanosystems were found to have a regular spatial pore distribution in the matrix volume. The filling of pores without breaking a matrix was shown to be maximal and uniform in Fe–SiO_2–350 and Fe–SiO_2–375 samples, and the iron nanoparticles in the pores were mainly in the γ phase of Fe_2O_3 with a small addition of the α phase and atomic iron clusters. Some iron atoms substitute for silicon atoms in the matrix at the matrix/nanofilament interface.

The data obtained allow us to conclude that, after annealing of the samples at $T = 350$–375°C, the iron oxide nanofilaments introduced in mesoporous silicon oxide have the optimum sizes and magnetic properties for using in data recording and storage systems with an ultrahigh density. The maximum anisotropy parameter is 45 ± 2, the coercive force is 54 ± 0.1 mT at $T = 4$ K and 22.0 ± 0.2 mT at $T = 300$ K, and the saturation magnetization is $(0.61 \pm 0.02) \times 4\pi \times 10^{-3}$ A m^2/kg at $T = 300$ K.

To describe the magnetic properties of the nanocomposites with an ordered structure of magnetic nanofilaments, we used the Preisach model and obtained satisfactory results, which agreed with the experimental data obtained by various techniques: the effective magnetic field acting on a nanofilament from other nanofilaments is 11 mT and has a dipole character, the ferromagnetic–paramagnetic transition temperature is in the range 76–94 K depending on the annealing temperature, and the magnetization reversal temperature of iron oxide nanofilaments is $T \approx 50$–60 K in a field $H = 0$ and $T \approx 80$ K in a field $H = 300$ mT.

The magnetic and structural properties of the spatially ordered magnetic nanocomposites were analyzed by SAPNS, which consists of nuclear and magnetic contributions and nuclear–magnetic interference. The distinctive attribute of this method is that, apart from scattering by individual particles (which gives integrated information for the entire sample), neutron scattering by a system of spatially ordered nanoparticles is also detected. In other words, the following two contributions to small-angle scattering are detected: diffraction by a regular pore structure and scattering by defects in individual nanoparticles, which makes it possible to characterize the systems under study in the area of at most 4–6 nm^2. It was shown that the nanocomposite materials based on a mesoporous silicon dioxide matrix with embedded iron oxide nanoparticles exhibited an unusual increase in the coherence during magnetization reversal in both positive and negative fields. In magnetic fields $H >$ 100 mT, coherent rotation of the magnetization of individual nanoparticles as an ensemble takes place. At $H < 100$ mT, the magnetization reversal of a system of magnetic nanofilaments occurs by analogy with a domain scenario: every nanofilament undergoes the influence of the effective field from other nanofilaments, which has dipole nature.

ACKNOWLEDGMENTS

We thank S. M. Sukharzhevskii (St. Petersburg State University) for the performance of the ESR experiments, A. V. Komolkin (St. Petersburg State University) for his help in processing the SQUID magnetometry data, and D. Yu. Chernyshov (European Synchrotron Radiation Facility, Grenoble, France) for his help in performing the synchrotron radiation diffraction experiments and processing the experimental results.

This work was supported by the Russian Foundation for Basic Research (project nos. 12-02-12066-ofi_m, 14-22-01113-ofi_m) and FTsP Kadry (project no. 2012-1.2.1-12-000-1010-051).

REFERENCES

1. A. K. Menon and B. K. Gupta, Nanostruct. Mater. **11**, 965 (1999).
2. L. Thomas, F. Lionty, R. Ballou, et al., Nature **383**, 145 (1996).

3. J. S. Beck, J. C. Vartuli, W. J. Roth, et al., J. Am. Chem. Soc. **114**, 10834 (1992).
4. G. De, L. Tapfer, M. Catalano, et al., Appl. Phys. Lett. **68**, 3820 (1996).
5. K. S. Napolsky, A. A. Eliseev, A. V. Knotko, et al., Mater. Sci. Eng. C **23**, 151 (2003).
6. J. Cheon, K.-B. Lee, H. Kang, et al., in *Proceedings of the MRS Symposium on Anisotropic Nanoparticles: Synthesis, Characterization and Applications, Boston, MA, 2000*, p. 635.
7. R. Zboril, M. Mashlan, and D. Petridis, Chem. Mater. **14**, 969 (2002).
8. R. Zboril, M. Mashlan, D. Krausova, et al., Hyperfine Interact. **120–121**, 497 (1999).
9. R. Skomskii and J. M. D. Coey, *Permanent Magnetism* (Inst. Phys., Bristol, UK, 1999).
10. R. D. Zusler, M. Vasquez-Mansilla, C. Arciprete, et al., J. Magn. Magn. Mater. **224**, 39 (2001).
11. C. G. Shull, W. A. Strauser, and E. O. Wollan, Phys. Rev. B **83**, 333 (1951).
12. C. Guilland, J. Phys. Radium. **12**, 489 (1951).
13. N. Amin and S. Arajs, Phys. Rev. B **35**, 4810 (1987).
14. A. B. Bourlinos, A. Simopoulos, and D. Petridis, Chem. Mater. **14**, 899 (2002).
15. G. Ennas, A. Musinu, G. Piccaluga, et al., Chem. Mater. **10**, 495 (1998).
16. C. Cannas, M. F. Casula, G. Concas, et al., J. Mater. Chem. **11**, 3180 (2001).
17. http://www.esrf.eu/computing/scientific/FIT2D/.
18. http://www.cdifx.univ-rennes1.fr/winplotr/.
19. C. P. Jaroniec, R. K. Gilpin, and M. Jaroniec, J. Phys. Chem. B **101**, 6861 (1997).
20. R. K. Iler, *The Chemistry of Silica* (Wiley, New York, 1979).
21. C. T. Hseih, W. L. Huang, and J. T. Lue, J. Phys. Chem. Solidi **63**, 733 (2002).
22. R. D. Shull, J. J. Ritter, and L. J. Swartzendruber, J. Appl. Phys. **69**, 5144 (1991).
23. B. Bleaney and K. W. H. Stevens, Rep. Progr. Phys. **16**, 108 (1953).
24. B. Bleaney, London, Edinburgh, Dublin Philos. Mag. J. Sci. **42**, 328 (1951).
25. A. Abraham and B. Bleaney, *Electron Paramagnetic Resonance of Transition Ions* (Clarendon, Oxford, 1970; Mir, Moscow, 1973).
26. S. R. Kurkjian and E. A. Sigety, Phys. Chem. Glass. **9**, 73 (1968).
27. V. V. Pan'kov, M. I. Ivanovskaya, and D. A. Kotikov, in *Chemical Problems of Creation of New Materials and Technologies,* Ed. by O. A. Ivashkevich (Belorus. Gos. Univ., Minsk, 2008), No. 3, p. 39 [in Russian].
28. H. K. Lachowicz, A. Sienkiewicz, P. Gierlowski, et al., J. Appl. Phys. **88**, 368 (2000).
29. R. Zysler, D. Fiorani, J.-L. Dormann, et al., J. Magn. Magn. Mater. **133**, 71 (1994).
30. M. M. Ibrahim, G. Edwards, M. S. Seehra, et al., J. Appl. Phys. **75**, 5873 (1994).
31. F. Gazeau, J.-C. Bacri, F. Gendron, et al., J. Magn. Magn. Mater. **186**, 175 (1998).
32. K. Parekh, R. V. Upadhyay, R. V. Mehta, et al., J. Appl. Phys. **88**, 2799 (2000).
33. L. Néel, J. Phys. Radium **15**, 224 (1954).
34. B. Martinez, X. Obradors, L. Balcells, et al., Phys. Rev. Lett. **80**, 181 (1998).
35. M. Respaud, J. M. Broto, H. Racoto, et al., Phys. Rev. B **57**, 2925 (1998).
36. F. Preisach, Z. Phys. **94**, 277 (1935).
37. T. Song and R. M. Roshko, IEEE Trans. Magn. **36**, 223 (2000).
38. E. C. Stoner and E. P. Wohlfarth, Phil. Trans. R. Soc. A **240**, 599 (1948).
39. S. V. Grigoriev, A. V. Syromyatnikov, A. P. Chumakov, et al., Phys. Rev. B **81**, 125405 (2010).
40. N. A. Grigorieva, S. V. Grigoriev, A. I. Okorokov, et al., Phys. E: Low-Dim. Syst. Nanostruct. **28**, 286 (2005).
41. S. V. Grigoriev, N. A. Grigor'eva, K. C. Napol'skii, A. P. Chumakov, A. A. Eliseev, I. V. Roslyakov, H. Eckerlebe, and A. V. Syromyatnikov, JETP Lett. **94**, 635 (2011).

Translated by K. Shakhlevich